Journal of Materials Chemistry A

PAPER

View Article Online
View Journal | View Issue

Check for updates

Cite this: J. Mater. Chem. A, 2018, 6, 20778

Pathways towards high performance Na–O_2 batteries: tailoring graphene aerogel cathode porosity & nanostructure†

Marina Enterría, [a] Cristina Botas, [a] Juan Luis Gómez-Urbano, [a] Begoña Acebedo, [a] Juan Miguel López del Amo,[a] Daniel Carriazo, [ab] Teófilo Rojo *[ac] and Nagore Ortiz-Vitoriano *[ab]

Fundamental understanding of the physical phenomena and electrochemical reactions occurring in metal–air batteries is critical for developing rational approaches towards high-performing Na–O_2 battery cathodes. In this context, air cathode porosity plays a key role in battery performance, influencing oxygen supply and hence oxygen reduction and evolution reaction kinetics (ORR/OER). Graphene-based aerogels offer great versatility as air-cathodes due to their low density, high electronic conductivity and adjustable porosity. Reduced graphene aerogels with different porosities are examined where high meso-macroporosity and a narrow macropore size arrangement exhibit the best electrode performance among all studied materials (6.61 mA h cm^{-2}). This is ascribed to the particular macroporous 3D structure of graphene-based electrodes, which favours the diffusion of oxygen to the defect sites in graphene sheets. An outstanding cycle life is achieved by using the pore-tuned cathode, leading to 39 cycles (486 h) at 0.5 mA h cm^{-2} with very low overpotential (250 mV) and efficiency over 95%. The cyclability is further increased to 745 h (128 cycles) by decreasing the capacity cut-off. This study shows that tuning of material porosity opens a new avenue of research for achieving Na–O_2 batteries with high performance by maximizing the effective area of the electrodes for the ORR/OER.

Received 27th July 2018
Accepted 21st September 2018

DOI: 10.1039/c8ta07273f

rsc.li/materials-a

Introduction

Rechargeable metal–oxygen (Li, Na) batteries are receiving a great deal of interest as possible alternatives to lithium-ion batteries, due to the inherent advantage that the active material in the cathode (O_2) is absorbed from the surrounding environment – giving these batteries some of the highest theoretical energy densities of all battery systems.[1] Since the beginning of the 21st century, much attention has been focused on aprotic lithium oxygen batteries (Li–O_2), the battery with the highest theoretical energy density. However, substantial challenges such as reversibility and cycle life must be addressed before widespread commercial implementation is possible.[2–10] Recently, a metal–air battery in which lithium is replaced by sodium has received increasing attention.[11] Sodium–oxygen (Na–O_2) batteries arise as a promising alternative due to key advantages of Na such as low cost, its abundance and higher ionic conductivities (relative to Li).[12,13] Although Na–O_2 batteries present lower gravimetric energies than Li–O_2 batteries on a cell basis (based on discharge products Na_2O_2/NaO_2: 1605/1108 W h kg^{-1}, respectively; Li_2O_2, 3505 W h kg^{-1}), much lower charge overpotentials than those in typical Li–O_2 batteries have been reported during discharge and charge (~100 mV *vs.* ~1000 mV), based on reversible sodium superoxide (NaO_2) formation.[14–16] In addition, Na–O_2 batteries have shown to exhibit energy efficiencies higher than 90%.[17]

Besides cell performance, the utilization of suitable cathode materials is a point of major concern as they are responsible for achieving efficient deposition of the discharge products. Porous carbon materials have been largely used as electrodes in different electrochemical storage technologies due to their low cost, high surface area, chemical stability and high conductivity.[18] Despite their non-porous nature and higher cost, graphene sheets (GSs) have attracted a great deal of attention during the last decade considering their very low density, high electrical (~10^3 S m^{-1}) and thermal conductivity (~5000 W $m^{-1}K^{-1}$), strong mechanical strength (42 N m^{-1}) and chemical stability.[13] Generally, reduced graphene oxide (rGO) is prepared through controllable oxidation of graphite, exfoliation into graphene oxide (GO) sheets and further chemical/thermal reduction. The elimination of surface oxygen groups leaves behind abundant structural defects (missing atoms) that serve

[a]CIC EnergiGUNE, Álava Technology Park, C/ Albert Einstein 48, 01510 Miñano, Spain. E-mail: nortiz@cicenergigune.com

[b]IKERBASQUE, Basque Foundation for Science, 48013 Bilbao, Spain

[c]Departamento de Química Inorgánica, Universidad del País Vasco UPV/EHU, P.O. Box 664, 48080, Bilbao, Spain. E-mail: teo.rojo@ehu.eus

† Electronic supplementary information (ESI) available. See DOI: 10.1039/c8ta07273f

as active sites for a great number of chemical reactions.[19] Thus, 2D few layer graphene flakes combining sp^2 hybridized carbon atoms (outstanding electrical conductivity), sp^3 atoms located in the edges of the sheets (active sites) and high theoretical surface area of 2630 $m^2\ g^{-1}$, make the graphene highly attractive for electrochemical energy storage and hence Na–O_2 batteries. Despite these highly attractive features, the accessibility of such a high surface area is limited by the tendency of GSs to restack due to van der Waals or capillary forces. The densification of graphene-based materials during its manipulation leads to a dramatic decrease of the active area which limits the molecular diffusion through the GSs,[20,21] challenging the effective use of GSs theoretically surface area. In this context, the self-assembly in an aqueous solution of 2D graphene-based sheets to form 3D nanomaterials prevents individual GSs from stacking which provides low-density materials with controlled porosity.[22]

The pores offer a pathway for access of O_2 molecules and optimize the hosting of the discharge products, NaO_2 particles, which consequently improves the capacity. By adjusting the porosity it may also be possible to eliminate the diffusional/kinetic limitations associated with the redissolution of discharge products, and increase the efficiency. These highly attractive materials are obtained by suitable dispersion of the GO in aqueous solution, gelling the dispersion by physical or chemical assembly and drying the obtained gel. Freeze-casting combined with supercritical drying (low temperature and low pressures) ensures the obtaining of robust structures since the formed ice crystals go directly from the solid to gas phase avoiding the high surface tension of liquid water, which can cause the structure collapse.[23]

In the present work, an easy and sustainable preparation procedure of different rGO aerogels was followed to use them directly as self-standing, binder-free cathodes for Na–O_2 batteries. Avoiding the utilization of a binder and/or conductive additive offers several advantages such as reduction of the total weight of the battery, which is essential to develop practical Na–O_2 batteries (lower fraction of inactive materials allow greater cell energy densities). As well, the utilization of binder polymers during electrode manufacture not only decreases the overall conductivity of the electrode but also blocks to some extent the cathode porosity, reducing the electrochemically active surface area.

The structure of the electrodes was tuned to obtain different porosity arrangements, which showed a major influence on the electrochemical performance. To our knowledge, a rational examination of this key descriptor, which is critical to maximize the Na–O_2 battery performance, has been scarcely approached[24,25] and, specifically, for graphene-based cathodes has yet to be studied. Sun *et al.*[24] prepared hierarchical meso-macro nanocast carbon sphere cathodes which showed remarkable performance; however, very low active material loading (0.3 mg cm^{-2}) and a binder was used for preparation. Moreover, the correlation between the performance and the pore size or volume was left unexplored. Yadegari *et al.*[25] reported the correlation between the discharge capacity, surface area and porosity of gasified (NH_3 or CO_2) carbon cathode materials. The gasification of these materials to modify the porous structure also changes the surface chemistry of the carbons avoiding a suitable evaluation of the effect of the pores. Hence, the introduced nitrogen or oxygen groups are known to catalyze the ORR. The lack of detailed studies in this context is therefore evident where a deep understanding of the electrochemical storage phenomena occurring at the electrode surface is crucial for the manufacture of advanced energy storage devices.

Experimental

Materials synthesis: air electrode preparation

GO suspensions were prepared by a modified Hummers' method.[26] Briefly, 240 mL of concentrated H_2SO_4 and 5 g of sodium nitrate ($NaNO_3$) were added slowly under vigorous stirring to a 3 L round bottom flask containing 5 g of graphite powder (IMERYS, TIMREX-SFG75). Then, 30 g of $KMnO_4$ was added to the reaction mixture while the flask was held in an ice bath, followed by stirring for 3 h at 30 °C. Afterwards, 1 L of H_2O_2 (3 v/v%) was added to the flask. The resulting graphite oxide was washed several times with ultra-pure water followed by centrifugation until neutral pH. Subsequently, it was sonicated for 1 h and centrifuged (3500 rpm, 30 min), after which any remaining solid was discarded and a concentrated GO suspension was obtained. The suspension was diluted with water to obtain concentrations of 4 and 2 g L^{-1}. After that, three different procedures were employed in order to obtain self-standing binder-free GO discs: (i) 60 mL of the GO suspension (2 g L^{-1}) were suddenly frozen in liquid nitrogen (−196 °C), (ii) 60 mL of the GO suspension (2 g L^{-1}) were slowly frozen in an ultrafreezer (−75 °C); both samples were freeze-dried in a Telstar LyoQuest freeze drier to achieve GO aerogels, (iii) a few millilitres of GO suspension (4 g L^{-1}) were drop-cast on silicon rubber and allowed to dry at room temperature under atmospheric pressure to obtain a GO film. Discs of 12 mm diameter were cut from the GO aerogels or film and thermally reduced by slow heating in a tubular furnace at 2 °C min^{-1} up to 800 °C for 1 h at 80 mL min^{-1} argon flow. The as-prepared round-shaped 12 mm rGO electrodes were denoted as: ArGO_N for the aerogel freezed at −196 °C, ArGO_U for the aerogel freezed at −75 °C and film for the rGO film.

Physicochemical and morphological characterization of graphene-based electrodes

An ASAP2020 adsorption analyser (Micromeritics) was used to measure N_2 adsorption–desorption isotherms at −196 °C in the relative pressure range 10^{-4} to 0.99. Samples were degassed at 250 °C for 3 h under vacuum. The specific surface area (S_{BET}) was calculated according to the Brunauer–Emmett–Teller (BET) method[27] from the nitrogen isotherms in the relative pressure range of 0.05–0.25. The *t*-plot method was used to obtain the external surface area (S_{EXT}) in the relative pressure range of 0.07–0.25. The total volume of micro-mesopores (V_T) was calculated as the amount of N_2 adsorbed at a relative pressure of 0.99. The pore size distribution (PSD) was determined by using a 2D-NLDFT heterogeneous surface method (equilibrium/desorption branch) and fitting with SAIEUS® software. For the

materials with thicknesses larger than 100 μm (aerogels), the apparent density (ρ_a) was calculated by weighing and measuring the dry rGO electrodes. In the case of the thinner materials (rGO film), the thickness was measured by cross-sectional SEM imaging for more accurate density calculations. An AccuPyc II 1340 pycnometer (Micromeritics) was used to measure the true density (ρ_t) of all the prepared electrodes. The equivalent mesopore and macropore sizes were estimated by using the above described parameters. To that end, a cylindrical and homogeneous shape of the pores was assumed and the following equations were used:

The total pore (V_P) volume of micro-meso and macropores was calculated by the formula:

$$V_P = \frac{1}{\rho_a} - \frac{1}{\rho_t} \quad (1)$$

where ρ_a is the apparent density (g cm^{-3}) and ρ_t is the true density (g cm^{-3}).

The average mesopore size (D_{meso}) and average macropore size (D_{macro}) were calculated as specified below:

$$D_{meso} = 4V_T/S_{BET} \quad (2)$$

where V_T is the total volume of micro-mesopores (cm^3 g^{-1}) calculated by N_2 physical adsorption at −196 °C and S_{BET} the BET surface area (m^2 g^{-1}).

$$D_{macro} = 4V_P/S_{EXT} \quad (3)$$

where V_P is the total pore volume of micro-meso macropores calculated by He pycnometry at RT (cm^3 g^{-1}) and S_{EXT} the external surface area of meso-macropores calculated using the *t*-plot from the N_2 isotherms.

Morphological characterization of the fresh and discharged electrodes was conducted by Scanning Electron Microscopy (SEM) using a FEI Quanta250 microscope operating at 20 kV. In the case of discharged electrodes, samples were transferred from an Ar-filled glove box to the SEM using an air-tight holder to avoid air exposure. Samples were washed with dried ethylene glycol dimethyl ether (DME) prior to SEM imaging.

The nature of the discharge products was further studied by Raman Spectroscopy and Nuclear Magnetic Resonance (NMR). Samples were washed with dried DME prior to Raman and NMR analysis. Raman spectra were recorded with a Renishaw spectrometer (Nanonics Multiview 2000) operating with an excitation wave-length of 532 nm, focused with a 50× long working distance objective. The spectra were obtained by performing 10 acquisitions with 10 s of exposure time of the laser beam to the sample. A silicon wafer was used for calibration. An in-house air-tight holder was used for the measurements. All magic angle spinning nuclear magnetic resonance (MAS-NMR) spectra were recorded with a WB Bruker Avance III 500 spectrometer working at a frequency ν_o = 132.29 MHz for ^{23}Na. The experiments were performed on samples spun at the magic angle with a 2.5 mm standard probe. The MAS frequency was set to 20 kHz in all cases. ^{23}Na spectra were referenced to a 0.1 M NaCl solution resonating at 0 ppm. The non-selective π/2 pulse duration was adjusted to 1.3 μs and the recycling delay set to 5 seconds.

Cell assembly and electrochemical characterization

The Na–O_2 cells consisted of a sodium metal anode and graphene-based materials as the oxygen electrode (1.13 cm^2, 1.5–2.5 mg$_{graphene}$). The electrodes were dried at 120 °C under vacuum for 24 h and transferred to an Ar-filled glove box (H_2O < 0.1 ppm, O_2 < 0.1 ppm, Jacomex, France) without exposure to air. Ethylene glycol dimethyl ether, ($C_4H_{10}O_2$, DME), (anhydrous, 99.5% Sigma Aldrich) was used as the electrolyte solvent and sodium perchlorate ($NaClO_4$, 98%, Sigma Aldrich) as the conducting salt. DME was dried over molecular sieves (3 Å, Sigma Aldrich) for one week and $NaClO_4$ under vacuum at 80 °C for 24 h. The electrolyte solution of 0.1 M $NaClO_4$ in DME was prepared in the glove box with a final water content below 20 ppm, determined using a C20 Karl Fischer coulometer (Mettler Toledo). A pressurized 2-electrode Swagelok-type cell was used for the galvanostatic measurements. The cells were dried overnight at 120 °C and transferred to the glovebox prior to assembly. Cell assembly consisted of 12 mm diameter sodium metal (Sigma Aldrich), a graphene-based electrode and Celgard H2010 separators (Celgard, USA, 13 mm diameter) soaked in 150 μl of electrolyte. A 12 mm diameter stainless steel mesh (Alfa Aesar) was used as the current collector. Following assembly, cells were pressurized with pure oxygen to ∼1 atm before the electrochemical measurements. Cells were rested at open circuit voltage (∼2.2–2.3 V *vs.* Na^+/Na) for 8 h prior to applying current using a Biologic-SAS VSP potentiostat. The discharge and charge experiments were performed at a current of 100 mA g^{-1} (∼150–210 μA cm^{-2}) with a potential cut-off between 1.8 and 3.2 V *vs.* Na^+/Na.

Results and discussion

Textural and morphological properties of the graphene-based electrodes

The morphology of the self-standing binder-free rGO cathodes was studied by Scanning Electron Microscopy (SEM) imaging (Fig. 1). The film presents a flat and uniform surface with no visible porosity (Fig. 1a) and a thickness around 12 μm as measured by cross-sectional SEM imaging (inset Fig. 1a). In contrast, the porous nature of the aerogels is confirmed where the ArGO_U electrode displays large platelet-like structures incorporating voids of ∼100 μm (Fig. 1b) while ArGO_N

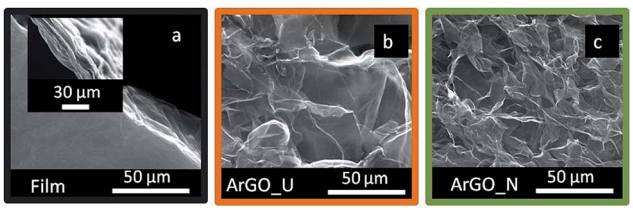

Fig. 1 SEM images of the rGO (a) film and aerogels, (b) ArGO_U and (c) ArGO_N. (Inset a) Cross-sectional SEM image of rGO film.

presents a smooth morphology with voids of around 30 μm (Fig. 1c). The appearance of narrow pores in ArGO_N is probably caused by the presence of small and randomly oriented aggregates of GSs formed during sudden freezing of the GO suspensions.

The textural properties of the rGO electrodes were studied in more detail by gas physical adsorption (Fig. 2 and Table 1). Fig. 2a displays the N_2 adsorption–desorption isotherms measured at −196 °C. As expected, rGO aerogels present larger pore volume than the film (Table 1). According to the International Union of Pure and Applied Chemistry (IUPAC) classification,[28] the film yields a type II isotherm which is ascribed to microporous solids with little contribution of mesopores. In contrast, ArGO_N and ArGO_U aerogels present type IV isotherms revealing the presence of both micro and mesopores. The electrode prepared by freeze-casting at lower temperature (ArGO_N) bear H3-type hysteresis indicating the presence of non-rigid aggregates of GSs bearing slit-shape pores in-between the sheets. The electrode freezed at −75 °C (ArGO_U) yields an H4 hysteresis loop indicating also the existence of interparticle porosity but narrow pore size.

Higher total pore volume (V_T) and specific surface (S_{BET}) and external areas (S_{EXT}) have been observed for the 3D porous aerogels when compared to that of the film (Table 1). The film, conversely, presents negligible gas adsorption in the whole pressure range and, consequently, can be considered a non-porous material. The slope of the isotherm curve at high-medium pressures is more pronounced for ArGO_N electrode than ArGO_U indicating a more developed micro-mesoporosity. The pore size distribution was further studied by NLDFT analysis (Fig. 2b). The aerogels present an adsorption maximum centered on 0.9 nm suggesting the presence of micropores where a much larger micropore volume is observed for ArGO_N. Most of the mesopores in ArGO_U are narrower than 5 nm while ArGO_N displays much wider mesopore size distribution, with sizes ranging from 5 to 25 nm. A larger average mesopore size and mesopore volume for the ArGO_N aerogel is further confirmed by calculating the equivalent mesopore diameter (Table 1, D_{meso}). Hence, the mesopore size shifts from 8.8 nm for ArGO_U to 11.3 nm for ArGO_N. The absence of saturation at high relative pressures ($P/P_0 = 1$) on the adsorption curves (Fig. 2a) reveals the presence of macropores larger than 100 μm.

Generally, the macroporosity in solid porous materials is studied by mercury intrusion porosimetry but the strong capillary forces applied during the analysis could lead to the collapse of the porous structure providing inaccurate results.[29] As far as we know, a method to study the macroporosity in graphene-based materials has not been already reported and, in order to analyze eventual differences in the macroporosity of the here prepared cathodes, a qualitative study combining He pycnometry at room temperature and N_2 adsorption at −196 °C was conducted in this work (Table 1). The apparent density (ρ_a) was calculated by measuring and weighing the electrodes while the true density (ρ_t, skeletal density with no contribution of pores) of the different samples was calculated by He pycnometry (Table 1). The high pore volume of aerogels is confirmed by their low apparent density (ρ_a) but large true density (ρ_t). ArGO_N presents the largest real density which confirms a greater pore volume for this sample (V_P, Table 1). In addition to the developed porosity, ArGO_N shows a narrower average macropore size (Table 1) than ArGO_U (1263 nm *vs.* 1630 nm).

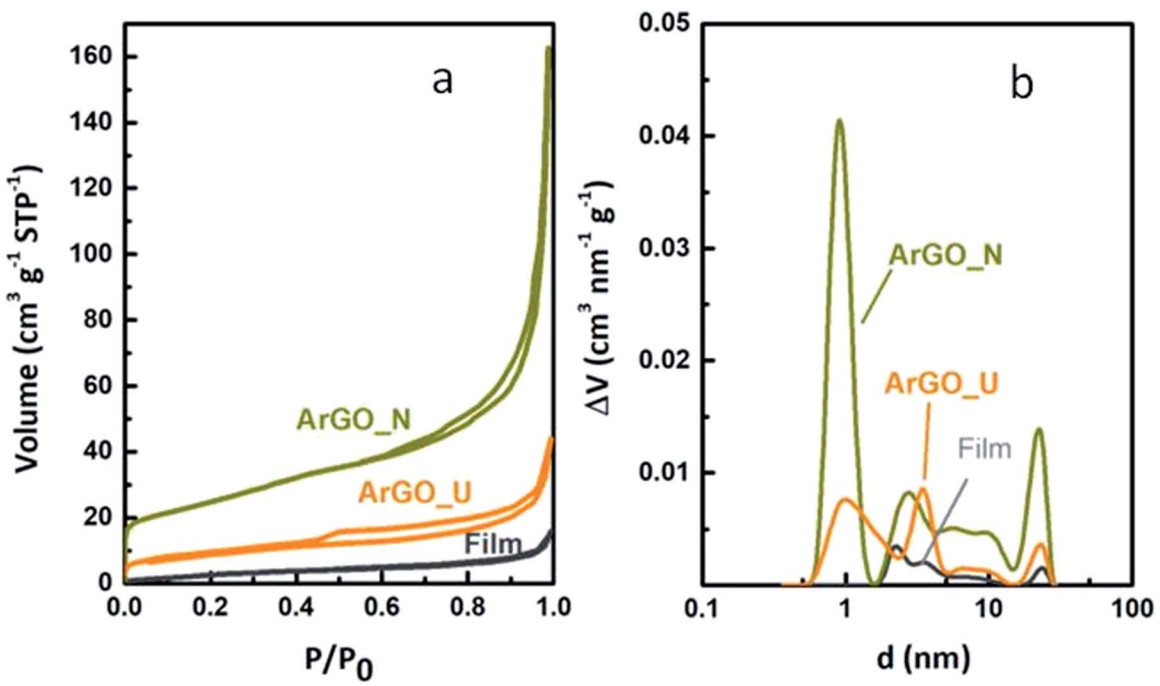

Fig. 2 (a) N_2 adsorption/desorption isotherms at −196 °C registered for the film, ArGO_N and ArGO_U and their (b) PSDs calculated from the adsorption isotherms by the 2D-NLDFT method.

Table 1 Textural parameters obtained from N_2 adsorption–desorption isotherms at −196 °C, and He pycnometry at room temperature. Total pore volume (V_P), equivalent mesopore size (D_{meso}) and equivalent macropore (D_{macro}) size calculations

	N_2 at −196 °C				He at RT			
	V_T ($cm^3\ g^{-1}$)	S_{BET} ($m^2\ g^{-1}$)	S_{EXT} ($cm^3\ g^{-1}$)	ρ_a ($g\ cm^{-3}$)	ρ_t ($g\ cm^{-3}$)	V_P[a] ($cm^3\ g^{-1}$)	D_{meso}[b] (nm)	D_{macro}[c] (nm)
Film	0.02	11	18	1.01	1.23	—	—	—
ArGO_U	0.07	32	35	0.07	1.85	14.3	8.8	1630
ArGO_N	0.22	78	65	0.05	2.14	20.5	11.3	1263

[a] Eqn (1). [b] Eqn (2). [c] Eqn (3).

A quick freezing of the GO suspension during the pore casting (ArGO_N) resulted in narrower macroporosity than that observed for a slow freezing (ArGO_U). The ice crystals formed during ArGO_N preparation are very small and highly dispersed as compared with the big crystals formed during the slow freezing. Regarding mesopores, the slow process provides time to the GO sheets to orientate leading to big aggregates (Fig. 1) and highly oriented mesoporous channels with narrow mesopore size distributions and large macropore size (Fig. 2b, Table 1). In contrast, a sudden freeze of the suspension resulted in randomly oriented small aggregates of GO sheets (Fig. 1) which gave rise to wide pore size distributions (Fig. 1b) with large mesopores and narrow macropores. The differences in the 3D structural arrangement of the GO sheets during the freeze-casting, therefore, not only lead to variations in the macroscopic morphology of the final electrodes by changing the aggregation behaviour of GSs but also in the pore size (nanoscale).

The as-prepared graphene-based materials present noticeable differences regarding porous properties which enable a suitable evaluation of the influence of this key parameter on Na–O_2 battery performance.

Electrochemical performance

We first examine the oxygen reduction reaction (ORR) kinetics of NaO_2 formation on graphene-based electrodes upon galvanostatic discharge. Fig. 3a shows the voltage profiles at a discharge rate of 100 mA g^{-1} to the full capacity. ArGO_U and film cathodes show large overpotentials (~300–400 mV; E^0 (NaO_2) = 2.27 V) and limited discharge capacities of 1.72 and 0.06 mA h cm^{-2}, respectively. ArGO_N, however, presents much higher discharge capacity (6.61 mA h cm^{-2}). The three studied materials present a similar potential drop at the beginning. This behaviour is related to the nucleation barrier needed to start the formation of the nucleation sites. Once these sites are available, the voltage increases and NaO_2 grows[30] around 2.01 V (2 mA h cm^{-2}) corresponding to an overpotential of only 260 mV for ARGO_N. The discharge stage ends with a sudden potential drop when NaO_2 covers the surface of the air cathode and there are no more active sites for NaO_2 growth.

Raman spectroscopy and ^{23}Na solid-state nuclear magnetic resonance (ssNMR) analysis were used to identify the nature of the discharge products (Fig. 3b and c, respectively). In the Raman spectra the presence of an intense peak centred at 1156 cm^{-1} for both ArGO_N and ArGO_U confirms NaO_2 as the main discharge product. This peak is also verified for the rGO film but features much lower intensity, probably due to the low capacity achieved (Fig. 3a). In addition, two broad peaks were observed at 1340 (D band) and 1585 (G band) cm^{-1}. The D-band is associated with the disordered structure of the graphene-based materials, representing the dispersive, sp3-bound induced vibrations, while the G-band is related to the vibration of sp2-bound carbon atoms. The intensity ratio (I_D/I_G) between these two peaks is largely used to estimate the concentration of defects in graphitic materials.[31] I_D/I_G ratios of *ca.* 1 were obtained for the different electrodes, pointing out the remaining graphitic character in all the samples, which favours

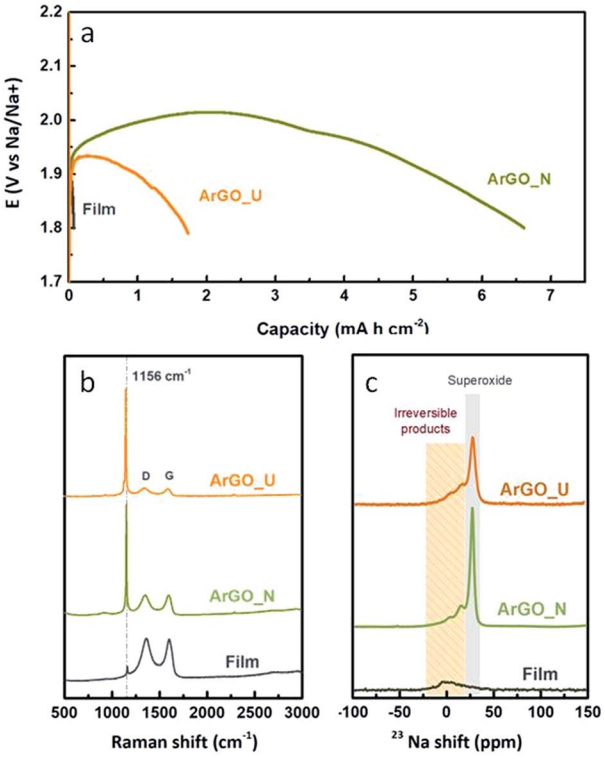

Fig. 3 (a) Voltage *versus* capacity of graphene-based electrodes discharged galvanostatically at 100 mA g^{-1} to full capacity in 0.1 M $NaClO_4$ in DME, (b) Raman spectra of the discharged electrodes. D and G bands of the graphene and the NaO_2 peak at 1156 cm^{-1} are indicated in the Raman spectra and (c) ^{23}Na ssNMR spectra for the discharged electrodes indicating the peaks of NaO_2 and irreversible products.

the electronic transport from/to the cathode.[32,33] Free-electrons located on lattice defects have been demonstrated to act as active sites for the ORR[13,34] as O_2 molecules oxidize preferentially at electron rich domains.[30] On the other hand, suitable porosity enhancing molecular diffusion is also crucial since O_2 molecules are adsorbed on the surface/pores of carbon-based air cathodes prior to the charge transfer process. Bearing this in mind, the low overpotential discharge verified for the ArGO_N cathode points out the enormous influence of the 3D arrangement of the GSs on the rGO aerogels when used as air electrodes.

Regarding NMR analysis, the ^{23}Na ssNMR spectra shown in Fig. 3c reveal that NaO_2 is the main discharge product. After discharge, ArGO_N and ArGO_U electrodes show a major resonance at −25 ppm attributed to NaO_2 [35] with two clear shoulders at around −16 and −5 ppm that can be ascribed to the formation of irreversible discharge subproducts.[36] The peak assigned to NaO_2 cannot be observed in the ^{23}Na-NMR spectra of the film since, as commented above, the discharge capacity is very low and the amount of NaO_2 might be below the detection limit.

The discharge product morphology was verified by SEM imaging (Fig. 4) where the cube-type morphology, characteristic of NaO_2 crystals, was found.[11,15] The amount of superoxide cubes observed for the porous aerogels is much larger than that of non-porous film due to the lower capacity of the latter (Fig. 3a). Both the number of cubes and the size (∼7 μm) are much lower for the film (Fig. 4a) than for the aerogel electrodes. The SEM images of the ArGO_U electrode (Fig. 4b) display a larger proportion of cubes as well as provide some relevant information; the NaO_2 cubes (∼11 μm) are preferentially distributed in the edge of the GSs (Fig. S1†) where high concentrations of defects are located. Hence, defects are thermodynamically unstable and high energy sites favouring the nucleation and trapping of metal oxide particles.[37] The deposition of NaO_2 on the ArGO_N cathode surface is greatly favoured, where the surface of the graphene-based sheets in the aerogel is fully covered with cubes of 11–20 μm size (Fig. 4c).

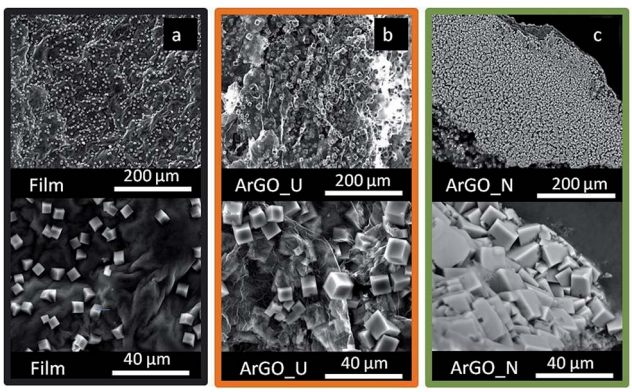

Fig. 4 SEM images of galvanostatically discharged graphene-based electrodes: (a) film, (b) ArGO_U and (c) ArGO_N, at the O_2/electrode interface (at 100 mA h g^{-1} to 1.8 V).

Considering that the amount of defect sites in the three studied rGO electrodes is similar (Fig. 3b), the effective utilization of those active sites must vary from one material to another. As compared with the film, the 3D arrangement of the GSs in the aerogel cathodes could expose a larger proportion of defects. Thus, the porous network acts as diffusion channel for an enhanced Na^+/O_2 supply while lower restacking of GSs provides accessible active sites (both sides of the sheets) for both the ORR and OER.[21,34] In addition, from discharge capacity results we observe that an interconnected porosity accommodates more efficiently the generated NaO_2 particles.

The influence of the electrode porosity on the cycling performance was then studied (Fig. 5) with the following procedure: Na–O_2 cells were discharged–charged at a current density of 100 mA g^{-1} (∼150–210 μA cm^{-2}) with a capacity cut-off of 0.5 mA h cm^{-2}. The capacity of the non-porous film is notably lower than the porous aerogels while the overpotential is much higher (Fig. 5a). ArGO_N presents much lower overpotential than ArGO_U (250 *vs.* 610 mV, at 0.2 mA h cm^{-2}).

After first cycle's stabilization, the average discharge and charge voltage plateaus of ArGO_N fall into the range of 2.04–2.12 V and 2.36–2.44 V, respectively. These values correspond to a charge overpotential of 240–370 mV (2nd to 38th cycle), which is substantially lower than those reported in the literature (see Table S1†) and hence better coulombic efficiency is achieved in this study. In addition, ArGO_N delivers 39 cycles (486 h) with 95–100% coulombic efficiency, followed by an overpotential increase (up to 510 mV at 39th cycle) and consequently capacity fade, probably due to accumulation of insoluble discharge products within the porous network (Fig. 5b and c). The ArGO_U electrode provides both lower cycle life (13 cycles; 183 h) and efficiency (85–95%, Fig. 5c) with a much higher overpotential 550 mV (13th cycle, Fig. S2a†). The overpotential increases dramatically, even in the 1st cycle when using the film cathode (∼530 mV, Fig. S2b†) and it is only able to discharge–charge 2 cycles up to 0.2 mA h cm^{-2} for 21 h (Fig. 5c). This finding further confirms the importance of building a tuned porous structure to achieve longer cycle life and stability.

In order to improve the cycle life of the ArGO_N cathode, a shallow-cycling experiment (0.15 mA h cm^{-2}) was further conducted (Fig. 6). The cycle life of the Na–O_2 battery increases from 39 cycles (0.5 mA h cm^{-2}) to 128 cycles (745 h) by decreasing the capacity cut-off (Fig. 6a). The morphology of the discharge products after cycling was further examined by SEM imaging (Fig. 6b). Two particle regimes are observed on the surface of ArGO_N; ∼12 μm cubes and ∼3 μm rounded particles; the latter particles were found to a greater extent. The appearance of different particle regimes might be due to the occurrence of two simultaneous processes; the dissolution of NaO_2 particles upon galvanostatic cycling (small particles) and appearance of new nucleation sites (big particles).

Table S1† summarizes the state-of-the-art Na–O_2 battery performance using graphene-based materials. We have included all relevant factors necessary for a fair comparison;[6,38] however, not always key parameters such as mass of active materials are given which hinders a reasonable evaluation. Among all the graphene materials reported in the

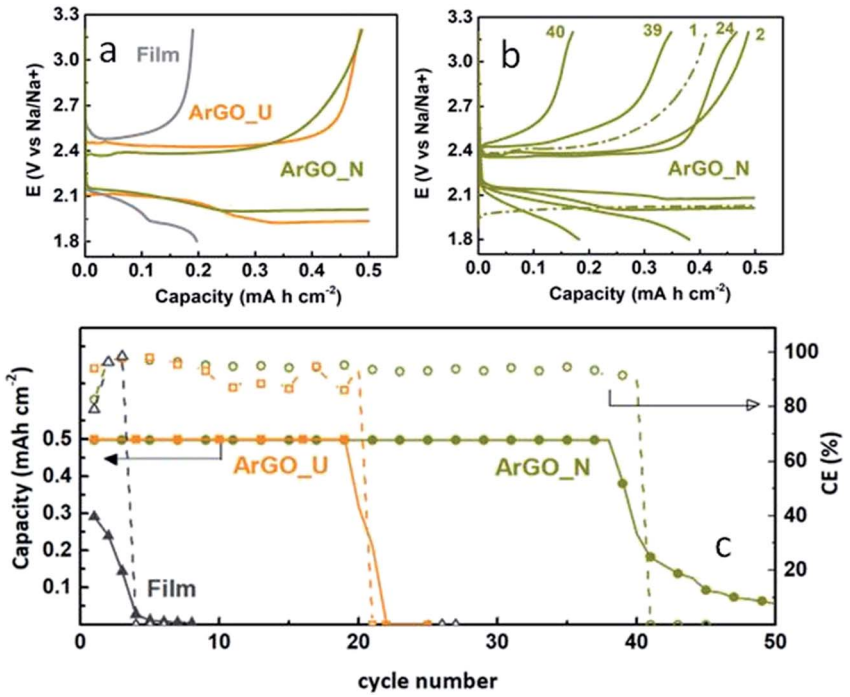

Fig. 5 (a) Second cycle discharge and charge voltage profiles of Na–O_2 cells to a fixed capacity (100 mA g^{-1} to 0.5 mA h cm^{-2} in 0.1 M $NaClO_4$ in DME) for the film and the aerogel electrodes (ArGO_U and ArGO_N), (b) cycling performance of the ArGO_N electrode and (c) evolution of discharge capacity (left axis, points denoted as filled symbols) and coulombic efficiency (right axis, points denoted as open symbols) with the number of cycles for all the studied electrodes (film, ArGO_U, and ArGO_N).

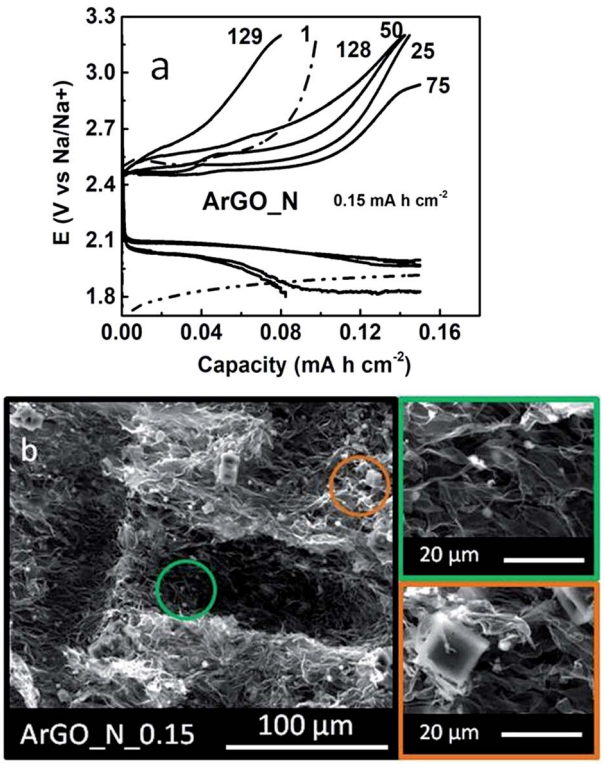

Fig. 6 (a) Cycling performance of ArGO_N at 100 mA g^{-1} to 0.15 mA h cm^{-2} in 0.1 M $NaClO_4$ in DME. (b) SEM images of the cycled electrode with the insets showing two selected areas corresponding to the two particle regimes.

literature,[36,39–43] the aerogels (this study) yield the highest mass of active material without addition of any binder. In addition, the concentration of the electrolyte is the lowest reported, which have been shown to affect the discharge capacity and overpotential, *i.e.*, a higher concentration of electrolyte gives rise to greater discharge capacities and lower overpotentials.[44] In order to verify this hypothesis, two ArGO_N electrodes (with similar mass, 0.52 *vs.* 0.73 mg) were discharged to full capacity in 0.1 and 1 M $NaClO_4$ DME electrolyte solutions (Fig. S3†). An increase in discharge potential can be observed at higher concentrations (2.18 V *vs.* 2.04 V at 1 mA h cm^{-2}) which supports the statement that lower overpotential is attained when using higher electrolyte concentrations. The discharge capacity, however, is lower when using 1 M concentration (2 *vs.* 6.6 mA h cm^{-2}). These findings suggest the need for further research to clarify this behaviour on different cathode materials. In addition, an enhanced discharge capacity is observed in this study when using a higher loading of active material, *i.e.*, graphene (Fig. S3†). A large amount of electrolyte could also decrease the overall energy density of the cell, hindering real implementation. In this work, even using the lowest concentration of electrolyte, the lowest charge overpotential has been attained (260 mV). Another factor worth considering is the working voltage; as broader voltage window will result in higher capacities. The voltage window in the literature is generally wider (1.8–3 V) than that of the current study (1.4 V).[39,40,42,43] Regarding the nature of the discharge products, most of the studies listed in Table S1† observed the formation of Na_2O_2 and Na_2CO_3 on the surface of the air cathode.[39–42] Nevertheless, the

formation of NaO_2 as the main discharge product has been observed to present lower overpotential and single flat plateau charge; the superoxide (NaO_2) is more reversibly oxidized to oxygen when compared with other discharge products.[45] Similar to the herein studied aerogel cathodes, only two studies identified the superoxide as the main discharge product.[36,43] Other attempts to improve the efficiency of NaO_2 cells include the addition of ORR/OER catalysts like noble metal nanoparticles[41,42] and transition metal oxides.[43] Even though such nanoparticles have demonstrated highly catalytic activity, they suffer from high cost, low selectivity, poor durability and detrimental environmental impact. The exploration for highly efficient, low-cost and more stable electrodes promoting the ORR/OER is a key issue for sustainable and competitive Na–O_2 batteries. In this context, metal-free carbon catalysts incorporating nitrogen atoms in the carbon lattice/bulk are a great alternative since heteroatoms can modify the acid/base and the electronic characteristic of the electrodes. Li *et al.* reported the preparation of nitrogen doped graphene nanosheets that, when used as Na–O_2 cell cathodes, performed only 3 cycles at 75 mA g^{-1} with a capacity cut off of 1150 mA h g^{-1}.[40] As well, the cell yields very poor efficiency as sodium peroxide (Na_2O_2) was observed as the main discharge product. The rGO sheets presented in this work, therefore, are demonstrated to be competitive with all the above commented approaches due to (i) the high conductivity and stability that graphene-based materials present and (ii) the existence of unpaired electrons located in lattice defects which can catalyse both the ORR and OER. When comparing with pure graphene-based materials our results are similar to those reported previously but with much higher mass content (0.15 *vs.* 1.5–2.5 mg), lower overpotential (400 *vs.* 260 mV) and longer cycling life when limiting the discharge capacity.[36,39] The approach herein presented does not require of complex procedures, expensive metals or functionalization/doping, providing an efficient and sustainable method for NaO_2 air cathode manufacture. Overall when comparing our result with current state of the art in terms of rate, discharge capacity and cycle life, the presented pore-tuned 3D graphene-based aerogel yields an outstanding performance as a Na–O_2 cathode. However, further studies to address the parasitic reactions while cycling are necessary to enhance the Na–O_2 battery performance which are currently in progress.

In addition, the influence of the pore size distribution of the present work correlates well with that reported for activated carbon Li–O_2 battery cathodes by Xiao *et al.*[46] They observed that both too large and too small pore sizes led to a less efficient use of mesopore volume. This observation is consistent with the conclusions extracted in this work since large mesopores existing in the ArGO_U cathode (>1500 nm) could lead to a loss of surface area for the adsorption of O_2 molecules and deposition of discharge products. As opposed to the trend observed in this work, Xiao's group reported that narrow pore size distributions with an average pore size ~3.5 nm enhance Li–O_2 batteries' efficiency. This might be due to the difference in cation size between Li and Na where Li ions could more easily access smaller pores than Na ions.[47] On the other hand, lithium presents higher desolvation energies than sodium and may need higher adsorption energies (narrower pores) to get desolvated for the formation of metal oxides.[48] The enhanced performance of the ArGO_N aerogel cathode as compared with

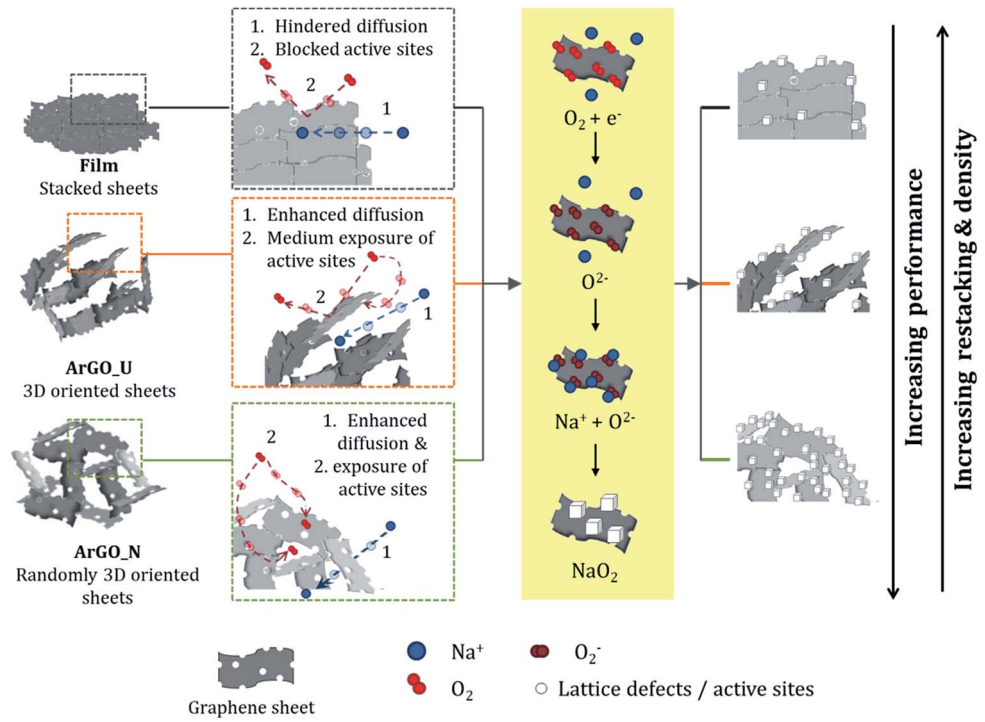

Scheme 1 Schematic illustration of the proposed mechanism as a function of the different 2D and 3D arrangements of GSs on the graphene-derived cathodes.

other carbon-derived electrodes is explained in Scheme 1, where the charge/discharge mechanism for the different studied materials is proposed. The electrochemically active area of 2D graphene-derived structures can be seriously reduced as restacking prevents the diffusion of O_2 molecules through the GSs. The subsequent formation of NaO_2 nuclei is therefore hindered (Fig. 4a) as the active sites are blocked in between the GSs. The fast capacity fade observed for the rGO film (Fig. 5c) may be caused by the absence of accessible active sites to perform the ORR/OER on the surface. Thus, a high overpotential is observed in the discharge–charge profile of film (Fig. S2b†) which confirms the inactivation of the active sites to perform the ORR/OER. The GSs in ArGO_U, however, form ordered domains by assembling in-between the oriented meso-macroporous channels (Fig. S4a†).

The thus formed porous network supplies a path for molecules to diffuse towards the active sites. Nevertheless, the oriented self-assembly of the sheets to form porous channels causes partial stacking, limiting the exposure of the active sites. The thus reduced effective area for oxygen to oxidation/reduction causes relative high overpotential (Fig. S2a†) and low cycling stability (Fig. 5c). In the case or ArGO_N, the disordered arrangement of the GSs (Fig. S4b†); (i) maximize the exposed surface of active sites, and (ii) provides large pore volume (0.22 $cm^3\ g^{-1}$), (iii) wide mesopore size distribution (5–25 nm) and (iv) narrow macropores size (~1200 nm). These specific features clearly promote the occurrence of the ORR/OER, enhance the molecular diffusion and favour the formation/redissolution of the NaO_2 cubes during the electrode cycling. It can therefore be concluded that the divergent performance of ArGO_N as compared with ArGO_U can be ascribed to the different spatial arrangement of the GSs and, consequently, to specific meso-macroporosity.

Conclusions

The porosity of rGO cathodes was tuned using a simple freeze-casting preparation procedure. Both the pore volume and pore size distribution of the obtained self-standing binder-free cathodes were tuned by simply changing the freezing temperature of GO precursor suspensions. The preparation of a non-porous film electrode enabled to verify the utility of a 3D pore-connected network. For the first time, it was observed that the discharge capacity and cyclability of Na–O_2 cells are strongly related to the porosity of the air-cathode. Hence, a sudden freeze at very low temperature of the GO suspensions (−196 °C) leads to a capacity of 6.61 mA h cm^{-2}, a good stability, and more than 100 cycles were obtained. The utilization of more progressive freezing (−75 °C) leads to significant reduction of both the discharge capacity and the cyclability. Such performance degradation is ascribed to large mesopores existing in the ArGO_U cathode (>1500 nm) which could lead to a loss of surface area for the adsorption of O_2 molecules and deposition of discharge products. The loss of the performance is evident when using a non-porous 2D rGO film as the cathode, highlighting the importance of a good interconnected graphene-based matrix for practical Na–O_2 batteries. The enhanced performance of the ArGO_N cathode is, therefore, related to three features; (i) highly accessible active sites for the ORR due to the tridimensional arrangement of GSs (low restacking), (ii) high pore volume (0.22 $cm^3\ g^{-1}$) and (iii) suitable mesopore (5–25 nm) and macropore (~1200 nm) size maximizing the surface area and molecules/ion diffusion. This work not only unravels the importance of obtaining 3D structures with interconnected pore channels but also opens a new avenue for the design of graphene-based cathodes with tailored properties to fulfill the Na–O_2 technology requirements.

Conflicts of interest

There are no conflicts to declare.

Acknowledgements

This work was financially supported by the European Union (Graphene Flagship, Core 2), the Spanish Ministry of Economy and Competitiveness (MINECO/FEDER) (MAT2015-64617-C2-2-R) and the Basque Government through ELKARTEK project CICE17. The authors thank Guillermo Liendo for assistance in NMR sample preparation.

Notes and references

1 K. Song, D. A. Agyeman, M. Park, J. Yang and Y.-M. Kang, *Adv. Mater.*, 2017, **29**, 1606572.
2 D. G. Kwabi, T. P. Batcho, C. V. Amanchukwu, N. Ortiz-Vitoriano, P. Hammond, C. V. Thompson and Y. Shao-Horn, *J. Phys. Chem. Lett.*, 2014, **5**, 2850–2856.
3 D. G. Kwabi, N. Ortiz-Vitoriano, S. A. Freunberger, Y. Chen, N. Imanishi, P. G. Bruce and Y. Shao-Horn, *MRS Bull.*, 2014, **39**, 443–452.
4 I. Landa-Medrano, I. Ruiz De Larramendi, N. Ortiz-Vitoriano, R. Pinedo, J. Ignacio Ruiz De Larramendi and T. Rojo, *J. Power Sources*, 2014, **249**, 110–117.
5 I. Landa-Medrano, R. Pinedo, N. Ortiz-Vitoriano, I. R. De Larramendi and T. Rojo, *ChemSusChem*, 2015, **8**, 3932–3940.
6 I. Landa-Medrano, R. Pinedo, I. R. de Larramendi, N. Ortiz-Vitoriano and T. Rojo, *J. Electrochem. Soc.*, 2015, **162**, A3126–A3132.
7 C. M. Burke, V. Pande, A. Khetan, V. Viswanathan and B. D. McCloskey, *Proc. Natl. Acad. Sci. U. S. A.*, 2015, **112**, 9293–9298.
8 B. D. McCloskey, C. M. Burke, J. E. Nichols and S. E. Renfrew, *Chem. Commun.*, 2015, **51**, 12701–12715.
9 C. Li, O. Fontaine, S. A. Freunberger, L. Johnson, S. Grugeon, S. Laruelle, P. G. Bruce and M. Armand, *J. Phys. Chem. C*, 2014, **118**, 3393–3401.
10 Y.-C. Lu, B. M. Gallant, D. G. Kwabi, J. R. Harding, R. R. Mitchell, M. S. Whittingham and Y. Shao-Horn, *Energy Environ. Sci.*, 2013, **6**, 750.
11 P. Hartmann, C. L. Bender, M. Vračar, A. K. Dürr, A. Garsuch, J. Janek and P. Adelhelm, *Nat. Mater.*, 2013, **12**, 228–232.
12 N. Ortiz-Vitoriano, N. E. Drewett, E. Gonzalo and T. Rojo, *Energy Environ. Sci.*, 2017, **10**, 1051–1074.

13 J. Xiao, D. Mei, X. Li, W. Xu, D. Wang, G. L. Graff, W. D. Bennett, Z. Nie, L. V. Saraf, I. A. Aksay, J. Liu and J. G. Zhang, *Nano Lett.*, 2011, **11**, 5071–5078.
14 I. Landa-Medrano, C. Li, N. Ortiz-Vitoriano, I. Ruiz De Larramendi, J. Carrasco and T. Rojo, *J. Phys. Chem. Lett.*, 2016, **7**, 1161–1166.
15 N. Ortiz-Vitoriano, T. P. Batcho, D. G. Kwabi, B. Han, N. Pour, K. P. C. Yao, C. V. Thompson and Y. Shao-Horn, *J. Phys. Chem. Lett.*, 2015, **6**, 2636–2643.
16 L. Lutz, W. Dachraoui, A. Demortière, L. R. Johnson, P. G. Bruce, A. Grimaud and J. M. Tarascon, *Nano Lett.*, 2018, **18**, 1280–1289.
17 H. Yang, J. Sun, H. Wang, J. Liang and H. Li, *Chem. Commun.*, 2018, **54**, 4057–4060.
18 R. C. Alkire, P. N Bartlett and J. Lipkowski, Electrochemistry of Carbon Electrodes, *Advances in Electrochemical Sciences and Engineering*, Wiley-VCH Verlag GmbH & Co., Weinheim, Germany, 2015.
19 C. Botas, P. Álvarez, P. Blanco, M. Granda, C. Blanco, R. Santamaría, L. J. Romasanta, R. Verdejo, M. A. López-Manchado and R. Menéndez, *Carbon*, 2013, **65**, 156–164.
20 M. Pumera, *Energy Environ. Sci.*, 2011, **4**, 668–674.
21 J. H. Lee, N. Park, B. G. Kim, D. S. Jung, K. Im, J. Hur and J. W. Choi, *ACS Nano*, 2013, **7**, 9366–9374.
22 S. Nardecchia, D. Carriazo, M. L. Ferrer, M. C. Gutiérrez and F. del Monte, *Chem. Soc. Rev.*, 2013, **42**, 794–830.
23 M. Enterría and J. L. Figueiredo, *Carbon*, 2016, **108**, 79–102.
24 B. Sun, K. Kretschmer, X. Xie, P. Munroe, Z. Peng and G. Wang, *Adv. Mater.*, 2017, **29**, 1606816.
25 H. Yadegari, Y. Li, M. N. Banis, X. Li, B. Wang, Q. Sun, R. Li, T. K. Sham, X. Cui and X. Sun, *Energy Environ. Sci.*, 2014, **7**, 3747–3757.
26 C. Botas, P. Álvarez, C. Blanco, R. Santamaría, M. Granda, P. Ares, F. Rodríguez-Reinoso and R. Menéndez, *Carbon*, 2012, **50**, 275–282.
27 *Adsorption by Powders and Porous Solids: Principles, Methodology and Applications*, ed. F. Rouquerol, J. Rouquerol and K. Sing, Elsevier, New York, 1999.
28 T. Matthias, K. Katsumi, V. N. Alexander, P. O. James, R. R. Francisco, R. Jean and S. W. Kenneth, *Physisorption of Gases, with Special Reference to the Evaluation of Surface Area and Pore Size Distribution (IUPAC Technical Report)*, 2015, vol. 87.
29 N. Job, R. Pirard, J. P. Pirard and C. Alié, *Part. Part. Syst. Charact.*, 2006, **23**, 72–81.
30 L. Lutz, D. A. D. Corte, Y. Chen, D. Batuk, L. R. Johnson, A. Abakumov, L. Yate, E. Azaceta, P. G. Bruce, J. M. Tarascon and A. Grimaud, *Adv. Energy Mater.*, 2018, **8**, 1701581.
31 M. A. Pimenta, G. Dresselhaus, M. S. Dresselhaus, L. G. Cancado, A. Jorio and R. Saito, *Phys. Chem. Chem. Phys.*, 2007, **9**, 1276–1290.
32 Y. Hou, J. Li, X. Gao, Z. Wen, C. Yuan and J. Chen, *Nanoscale*, 2016, **8**, 8228–8235.
33 Z. Ma, L. Tao, D. Liu, Z. Li, Y. Zhang, Z. Liu, H. Liu, R. Chen, J. Huo and S. Wang, *J. Mater. Chem. A*, 2017, **5**, 9412–9417.
34 E. Yoo and H. Zhou, *ACS Nano*, 2011, **5**, 3020–3026.
35 T. R. Krawietz, D. K. Murray and J. F. Haw, *J. Phys. Chem. A*, 1998, **102**, 8779–8785.
36 T. Liu, G. Kim, M. T. L. Casford and C. P. Grey, *J. Phys. Chem. Lett.*, 2016, **7**, 4841–4846.
37 *Graphene Materials: Fundamentals and Emerging Applications*, ed. A. Tiwari and M. Syväjärvi, John Wiley & SonsWiley, New Jersey, 2015.
38 S. A. Freunberger, *Nat. Energy*, 2017, **2**, 17091.
39 W. Liu, Q. Sun, Y. Yang, J.-Y. Xie and Z.-W. Fu, *Chem. Commun.*, 2013, **49**, 1951.
40 Y. Li, H. Yadegari, X. Li, M. N. Banis, R. Li and X. Sun, *Chem. Commun.*, 2013, **49**, 11731.
41 S. Zhang, Z. Wen, K. Rui, C. Shen, Y. Lu and J. Yang, *J. Mater. Chem. A*, 2015, **3**, 2568–2571.
42 S. Kumar, B. Kishore and N. Munichandraiah, *RSC Adv.*, 2016, **6**, 63477–63479.
43 F. Wu, Y. Xing, J. Lai, X. Zhang, Y. Ye, J. Qian, L. Li and R. Chen, *Adv. Funct. Mater.*, 2017, **27**, 1700632.
44 J. Hedman, Characterization of Reaction Products in Sodium-oxygen Batteries, Doctoral dissertation, University of Uppsala, 2017.
45 V. S. Dilimon, C. Hwang, Y. G. Cho, J. Yang, H. D. Lim, K. Kang, S. J. Kang and H. K. Song, *Sci. Rep.*, 2017, **7**, 17635.
46 J. Xiao, D. Wang, W. Xu, D. Wang, R. E. Williford, J. Liu and J. G. Zhang, *J. Electrochem. Soc.*, 2010, **157**, A487.
47 P. Serras, V. Palomares and T. Rojo, in *Alkali-ion Batteries: High-voltage Cathodes for Na-ion Batteries: Sodium–Vanadium Fluorophosphates*, ed. D. Yang, InTech, London, 2016, pp. 155–172.
48 K. L. Browning, R. L. Sacci and G. M. Veith, *J. Electrochem. Soc.*, 2017, **164**, A580–A586.